Electronic Supplementary Information

Controlled synthesis of Cu,Fe dual-atom catalysts restrained on metal-organic frameworks for efficient O_2 activation

Qi Xue[a,+], Ching Kit Tommy Wun[a,+], Tianxiang Chen[a,+], Shogo Kawaguchi[b], Sarah Day[c], Chiu Tang[c], Tai-Sing Wu[d], Yun-Liang Soo[e], Cong Lin[f], Yung-Kang Peng[g], Jun Yin*[h], Tsz Woon Benedict Lo*[a, h, i]

[a.] *Dr. Q. Xue, C. K. T. Wun, Dr. T. Chen, Dr. T. W. B. Lo**
Department of Applied Biology and Chemical Technology
The Hong Kong Polytechnic University
Hunghom, Hong Kong, China
E-mail: benedict.tw.lo@polyu.edu.hk
[b.] *Dr. S. Kawaguchi*
Japan Synchrotron Radiation Research Institute (JASRI), SPring-8, 1-1-1 Kouto, Sayocho, Sayo-gun, Hyogo 679-5198, Japan
[c.] *Dr. S. Day, Prof. C. Tang*
Diamond Light Source Ltd.
Harwell Campus, Oxford, OX11 0DE, United Kingdom
[d.] *Dr. T.-S. Wu*
National Synchrotron Radiation Research Center
101 Hsin-Ann Road, Hsinchu 30076, Taiwan
[e.] *Prof. Y.-L. Soo*
Department of Physics
National Tsing Hua University, Hsinchu 30013, Taiwan
[f.] *Dr. Cong Lin*
Department of Mechanical Engineering
The Hong Kong Polytechnic University
Hunghom, Hong Kong, China
[g.] *Dr. Y.-K. Peng*
Department of Chemistry
City University of Hong Kong
Hong Kong, China
[h.] *Dr. J. Yin*, Dr. T. W. B. Lo**
Department of Applied Physics
The Hong Kong Polytechnic University
Hunghom, Hong Kong, China
E-mail: jun.yin@polyu.edu.hk
[i.] *Dr. T. W. B. Lo**
The Hong Kong Polytechnic University Shenzhen Research Institute
The Hong Kong Polytechnic University
Shenzhen, 518057, China
† These authors contributed equally to this work as joint first authors.

Experimental Procedures

1. Experimental Procedures

Synthesis of UiO-66-NH_2

The synthesis procedure is according to the previously reported UiO-66-NH_2 with the structural formula of $Zr_6O_4(OH)_4(ATA)_{5.8}$ (ATA = 2-aminoterephthalic acid).[1] 0.240 g zirconium tetrachloride and 0.186 g ATA were dissolved in 20 mL N,N-dimethylformamide (DMF). The solution was transferred into a 100 mL hydrothermal vessel and heated at 120 °C for 12 hours. The UiO-66-NH_2 powder was collected by centrifugation and washed with water 5 times. Dried at 60 °C overnight.

Synthesis of Cu^{2+}-UiO-66-NH_2

A related modular approach has been used in our previous study to synthesise Cu_2 and Cu_3 clusters supported on the Zr_6O_4 secondary building units of UiO-66-NH_2.[2,3] 0.57 g UiO-66-NH_2 were dispersed in 20 mL H_2O by ultrasonication. 138.35 µL bis(ethylenediamine)copper(II) hydroxide was dropwise added. The mixture was stirred at room temperature for 3 hours. The product was collected by centrifugation and washed with 10 mL of double distilled water. It was dried at 70 °C overnight to obtain the product u^{2+}-UiO-66-NH_2.

Synthesis of Fe^{3+}-UiO-66-NH_2

0.57 g UiO-66-NH_2 were dispersed in 20 mL H_2O by ultrasonication, then 0.28 g $Fe(NO_3)_3$ was added. The mixture was stirred at room temperature for 3 hours to obtain Fe^{3+}-UiO-66-NH_2. The product was collected by centrifugation and washed with 10 mL douof ble distilled water.

Synthesis of Cu^{2+}-mIem-Fe^{3+}-UiO-66-NH_2

0.57 g Cu^{2+}-UiO-66-NH_2 were dispersed in 20 mL H_2O. 0.057 g 2-methylimidazole was added and reacted for 3 h. The solid sample was collected by centrifugation by 3 times and washed by double distilled H_2O to obtain mIem-Cu^{2+}-UiO-66-NH_2 in 20 mL H_2O. 0.28 g $Fe(NO_3)_3$ was then added and reacted at room temperature for 3 h to obtain Fe^{3+}-mIem-Cu^{2+}-UiO-66-NH_2. The sample was washed by double distilled H_2O by 3 times and dried at 70 °C.

*Synthesis of **Cu_1-UiO**, **Fe_1-UiO**, and **Cu,Fe-UiO***

Cu^{2+}-UiO-66-NH_2, Fe^{3+}-UiO-66-NH_2, and Cu^{2+}-mIem-Fe^{3+}-UiO-66-NH_2 are heated at 180 °C for 1 h with a heating rate of 10 °C/min. By calcination of the samples at 180 °C, the organic meIm linker can be removed. The vacant coordination sites are reactive which are hence stabilised by the neighbouring O atoms

Photocatalytic styrene oxidation

2.5 mg catalysts were dispersed in 1.5 mL 1,2-dichloroethane. 0.5 mL styrene was added and reacted in air for 30 min under UV irradiation (365 nm). The products were analysed by gas chromatography–mass spectrometry (GC-MS; Agilent).

2. Methods

High-resolution synchrotron X-ray powder diffraction (PXRD) and Rietveld refinement

High-resolution synchrotron PXRD data were collected at Beamline BL02B2, SPring-8, Japan. The energy of the incident X-ray flux was optimised at 17.8 keV or 18.0 keV. The tuned energy for each beamline emits the optimum X-ray flux to achieve high contrast (signal-to-noise ratio) and high angular resolution. The wavelength and the 2θ-zero point were calibrated using a diffraction pattern obtained from a high-quality standard CeO_2 powder (NIST SRM674b). High-resolution synchrotron PXRD data were obtained from the MOF samples (loaded in 0.5-mm borosilicate capillaries) using the MYTHEN detector. Each diffraction pattern was collected for an hour for good statistics. In total, there are 490 *hkl* reflections measured (within the region of refinement (2θ = 2-60°), of which at least 100 independent *hkl* reflections are observed. From a mathematical perspective, the number of variables should not exceed the number of observables. In the Rietveld refinements performed in this work, the number of structural parameters has not exceeded 40.

Using the TOPAS 6.0 software, the lattice parameters were obtained using Pawley and Rietveld refinement analyses of the diffraction patterns were performed. The background curve was fitted by a Chebyshev polynomial with an average of 16 coefficients. The Thompson-Cox-Hastings (pseudo-Voigt) function was applied to describe the diffraction peaks[4]. The scale factor and lattice parameters were allowed to vary for all the histograms.

The final refined structural parameters for each data histogram were carried out using the Rietveld method with the fractional coordinates (*x, y, z*) and isotropic displacement factors (B_{eq}) for all atoms. In addition, the R_{wp} and *goodness-of-fit* values (*gof* = R_{wp}/R_{exp}) are helpful to indicate the quality of fit, where R_{exp} represents the quality of the data.

In-situ synchrotron PXRD

Pre-treated samples were finely sieved and loaded in 0.5-mm-borosilicate capillaries to reduce the X-ray absorption problem. Dynamic measurements were conducted at a ramping rate of 5 °C min^{-1}. Each SXRD pattern required 10 min of scanning time for a suitable and reliable signal-to-noise ratio.

Extended X-ray absorption fine structure spectroscopy

The extended X-ray absorption fine structure (EXAFS) spectroscopy data were collected at BL07A at Taiwan Light Source using transmission mode, with an average scanning time of 20 minutes. Artemis and Athena software were used for data treatment and analysis.[5] The detailed fitting parameters are summarized in the caption of the EXAFS fittings. The Hamma software was used for wavelet transform[6].

Fourier-transform Infrared (FTIR) spectroscopy

FTIR spectroscopy experiments were performed in Thermo Scientific Nicolet IS50 with attenuated total reflection (ATR) mode. Probe-assisted samples were by adsorbing 30 µL styrene.

Electrochemical measurements

All linear sweep spectroscopic measurements were carried out on CHI 760D electrochemical workstation at room temperature in a standard three-electrode system. The samples were dispersed in the solution (water:ethanol:5wt%nafion of 1:1:0.02) to reach the concentration of 5 mg mL^{-1}. 20 µL solution with samples was added onto the surface of the glass carbon electrode and dried at room temperature. The electrochemical measurements were performed in 0.1 M KOH or 0.5 M H_2SO_4. A standard saturated calomel electrode (SCE) was used as the reference electrode and all potential values in this work were normalized to the normal hydrogen electrode (RHE). A glass carbon electrode with a diameter of 3 mm and length of 8 cm was used as the counter electrode.

Computational methods

Density functional theory (DFT) calculations were performed using the projector-augmented wave (PAW) method as implemented in the Vienna Ab initio Simulation Package. The generalised gradient approximation (GGA) with the Perdew-Burke-Ernzerhof (PBE) exchange-correlation functional was used. The 1×1×1 k-mesh grid in the Brillouin zone was employed to optimise the geometries of Cu,Fe-UiO cluster model before and after interacting with styrene, as well as the hypothetical Cu,Cu-UiO cluster model. The plane-wave basis set cutoff of the wave functions was set at 450 eV for all the structures. The atomic positions of all structures were fully relaxed until the supercells had forces on each atom less than 0.015 eV/Å. The binding energies were calculated using the equations of $E_{binding} = E_{total} - E_{Cu,Fe\text{-}UiO} - E_{O2}$ and $E_{binding} = E_{total} - E_{Cu,Cu\text{-}UiO} - E_{O2}$.

Results and Discussion

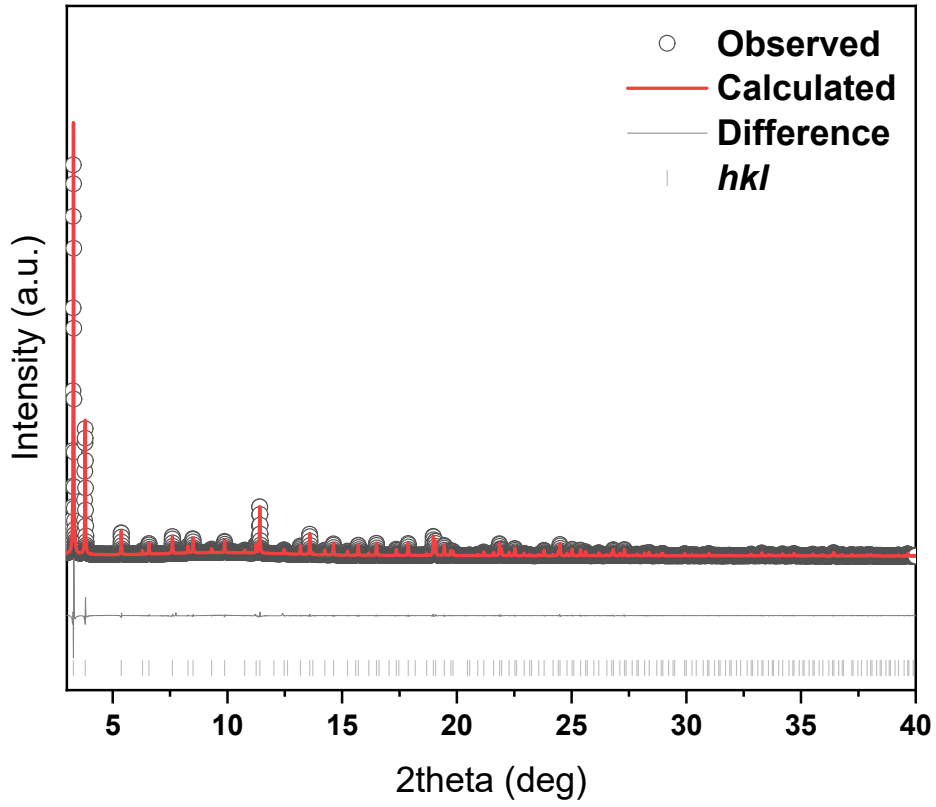

Figure S1. High-resolution synchrotron X-ray powder diffraction data of UiO-66-NH_2 collected on Beamline BL02B2 at SPring-8. The X-ray energy was optimised at 17.8 keV.

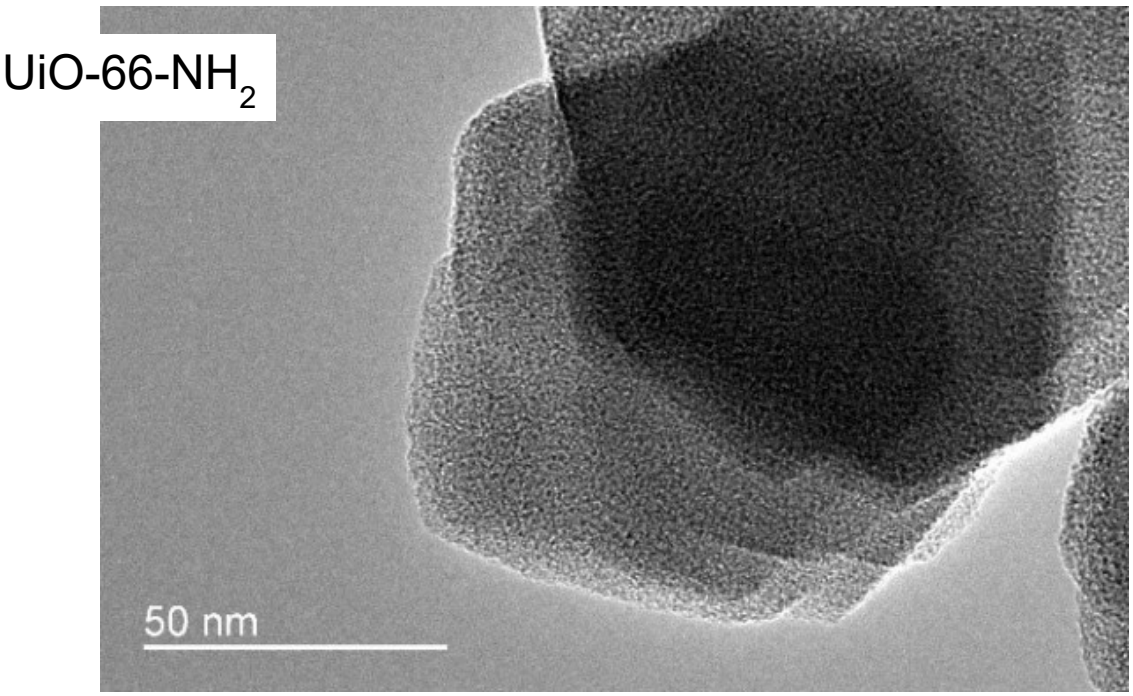

Figure S2. Transmission electron microscopy image of pristine UiO-66-NH_2 on Ni grid.

T**able S1.** The elemental analysis, showing the Zr: metal atomic ratio, of **Cu_1-UiO**, **Fe_1-UiO**, and **Cu,Fe-UiO** by SEM/EDX.

	Zr	**Cu**	**Fe**
Cu_1-UiO	1	0.091	-
Fe_1-UiO	1	-	0.039
Cu,Fe-UiO	1	0.069	0.074

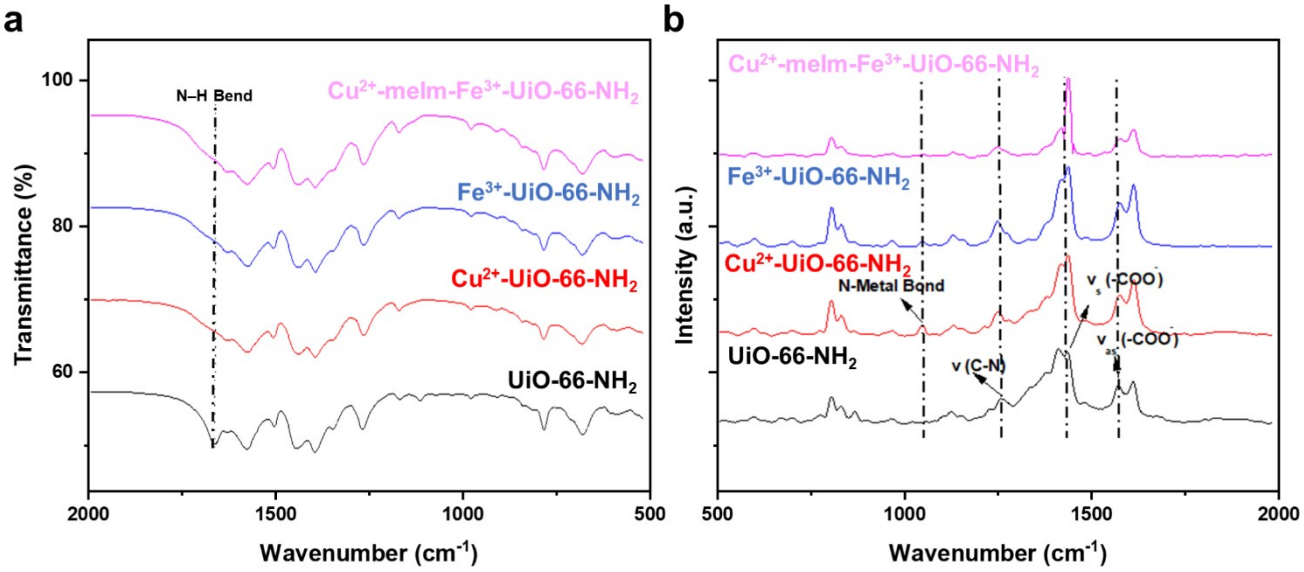

Figure S3. (**a**) Fourier-transform infrared and (**b**) Raman spectroscopic study of the non-calcined (precursor) samples, i.e., Cu^{2+}-, Fe^{3+}-, and Cu^{2+}-meIm-Fe^{3+}-UiO-66-NH_2.

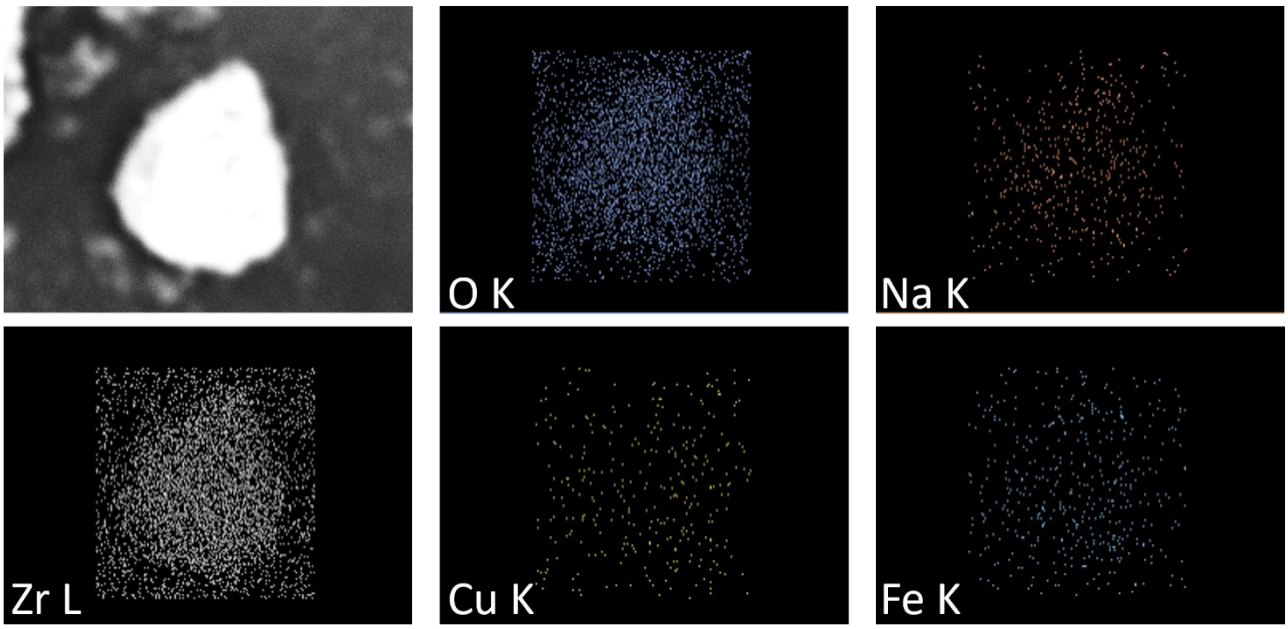

Figure S4. Scanning electron microscopy/energy-dispersive X-ray spectroscopy (SEM/EDX) mapping analysis of **Cu,Fe-UiO** showing the homogeneous distribution of Cu and Fe within a UiO-66-NH_2 nanocrystallite.

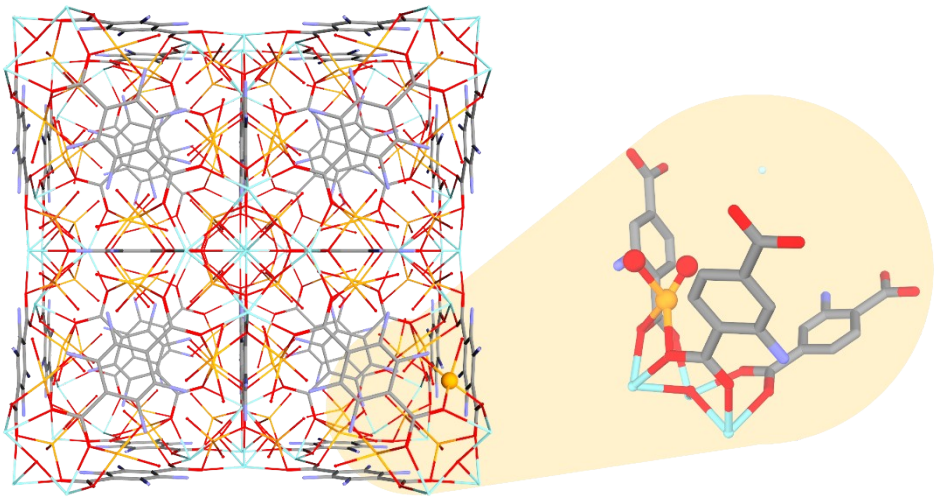

Figure S5. Rietveld refined crystal structure of **Fe_1-UiO** as synthesised before.[1]

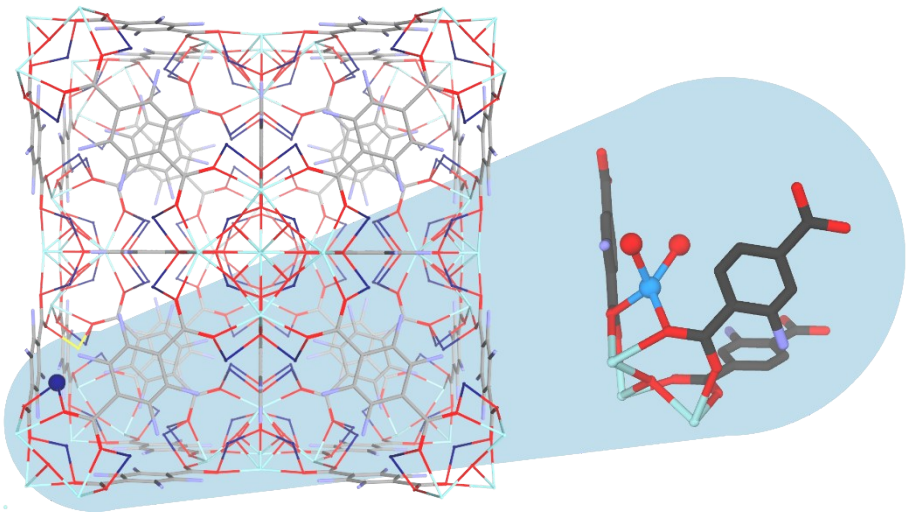

Figure S6. Rietveld refined crystal structure of **Cu_1-UiO** as synthesised before.[7]

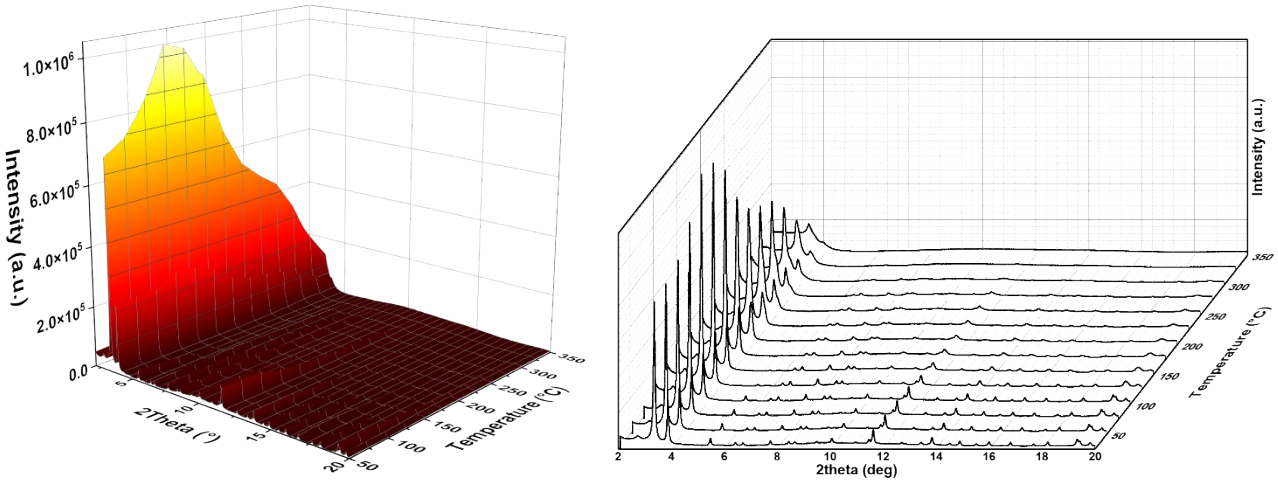

Figure S7. *In-situ* synchrotron PXRD showing the dynamic change of Cu^{2+}-meIm-Fe^{3+}-UiO-66-NH_2 in the diffraction profiles at elevated temperatures. Data was collected on Beamline BL02B2 at SPring-8, at the X-ray energy of 17.8 keV.

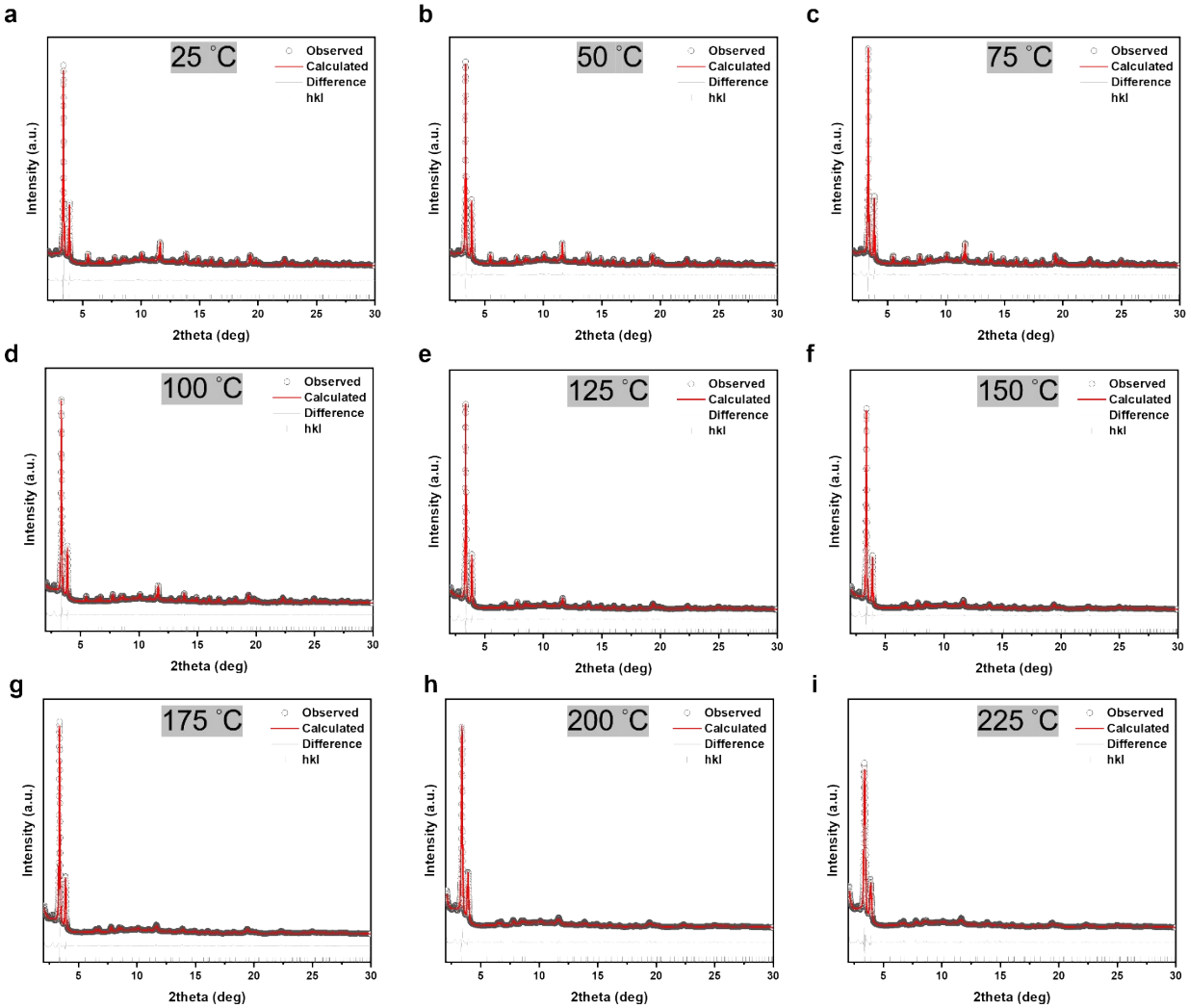

Figure S8. Pawley refinement profiles of *in-situ* synchrotron PXRD data.

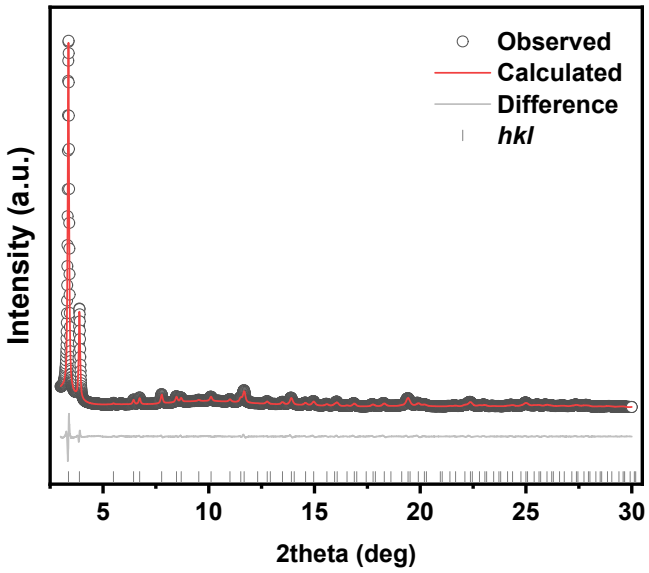

Figure S9. High-resolution synchrotron PXRD of **Cu,Fe-UiO**, and the corresponding Pawley refinement profile. Data was collected on Beamline BL02B2 at SPring-8. The X-ray energy was optimised at 17.8 keV.

Table S2. Crystallographic parameters derived from the synchrotron PXRD measurements of samples as labelled.

	UiO-66-NH_2	Cu^{2+}-meIm-Fe^{3+}-UiO-66-NH_2	**Cu,Fe-UiO**	**Cu,Fe-UiO (post-mortem)**
Diffractometer	MYTHEN	MYTHEN	MYTHEN	Dectris 1D area detector
X-ray source	SPring-8 BL02B2	SPring-8 BL02B2	SPring-8 BL02B2	Rigaku SmartLab SE
Wavelength (Å)	0.688213(2) (Synchrotron)	0.700261(2) (Synchrotron)	0.700261(2) (Synchrotron)	0.71073 (Mo X-ray)
2θ - zero point (°)	-0.000106(2)	0.00037	0.00037	0.0009(1)
Space group	*Fm-3m*	*Fm-3m*	*Fm-3m*	*Fm-3m*
Crystal system	Cubic	Cubic	Cubic	Cubic
a (Å)	20.78902(46)	20.7559(30)	20.75787(29)	20.7341(30)
V ($Å^3$)	8984.66(59)	8766.4(17)	8944.3(4)	8913.7(1)
2θ range for refinement (°)	2-30	2-30	2-30	2-30
Refinement methods	Rietveld	Rietveld	Rietveld	Rietveld
$R_{wp}/R_{exp}/R_p$ (%)	2.258/0.777/1.553	5.672/0.618/4.28	5.840/0.674/4.192	10.928/8.620/8.578
gof	2.905	9.171	8.668	1.267

R_{wp}: weighted profile; R_{exp}: expected; R_p: profile; *gof:* goodness-of-fit. The wavelengths and zero-point errors were calibrated by NIST CeO_2 standard.

Table S3. Crystallographic parameters derived from the *in-situ* synchrotron PXRD measurements at elevated temperatures of Cu^{2+}-meIm-Fe^{3+}-UiO-66-NH_2.

Temperature (°C)	**R_{wp} (%)**	**R_{exp} (%)**	**R_p (%)**	**Lattice parameter (Å)**
25	4.61	0.638	3.13	20.7559(30)
50	4.31	0.639	3.06	20.751(29)
75	5.45	0.629	3.81	20.725(38)
100	4.38	0.636	3.14	20.728(30)
125	5.30	0.617	3.78	20.692(28)
150	5.43	0.617	4.02	20.659(20)
175	5.67	0.618	4.28	20.619(14)
200	5.55	0.618	4.21	20.554(22)
225	5.91	0.617	4.52	20.497(30)
250	7.95	0.617	5.66	20.49(5)
275	8.38	0.616	5.23	20.53(5)
300	7.10	0.617	4.34	20.50(5)
325	2.77	0.619	2.04	20.24(5)
350	1.92	0.620	1.44	20.13(9)

R_{wp}: weighted profile; R_{exp}: expected; R_p: profile.

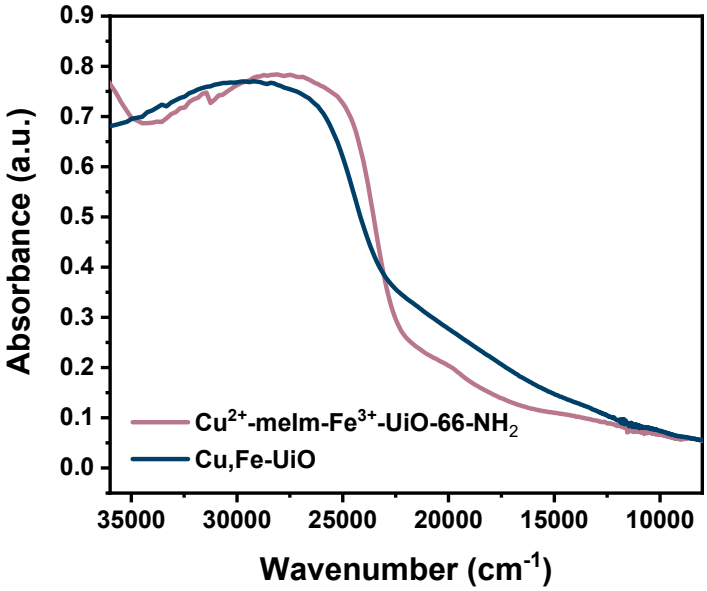

Figure S10. UV-vis-NIR spectra of Cu^{2+}-meIm-Fe^{3+}-UiO-66-NH_2 (precursor of **Cu,Fe-UiO**), and **Cu,Fe-UiO**, showing the effect of calcination.

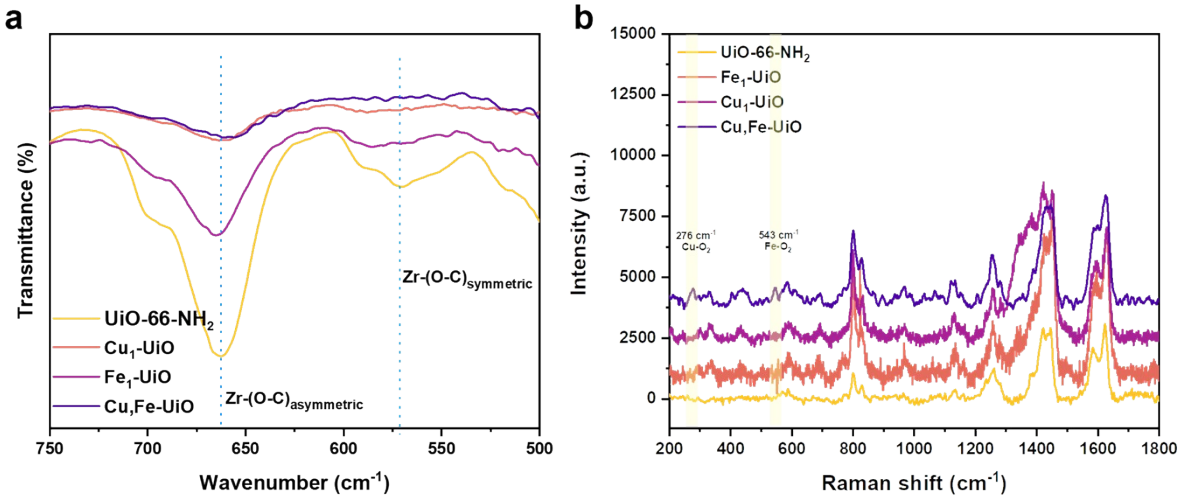

Figure S11. (**a**) UV-vis-NIR spectra and (**b**) Raman spectra of UiO-66-NH_2, **Fe_1-UiO**, **Cu_1-UiO**, and **Cu,Fe-UiO**

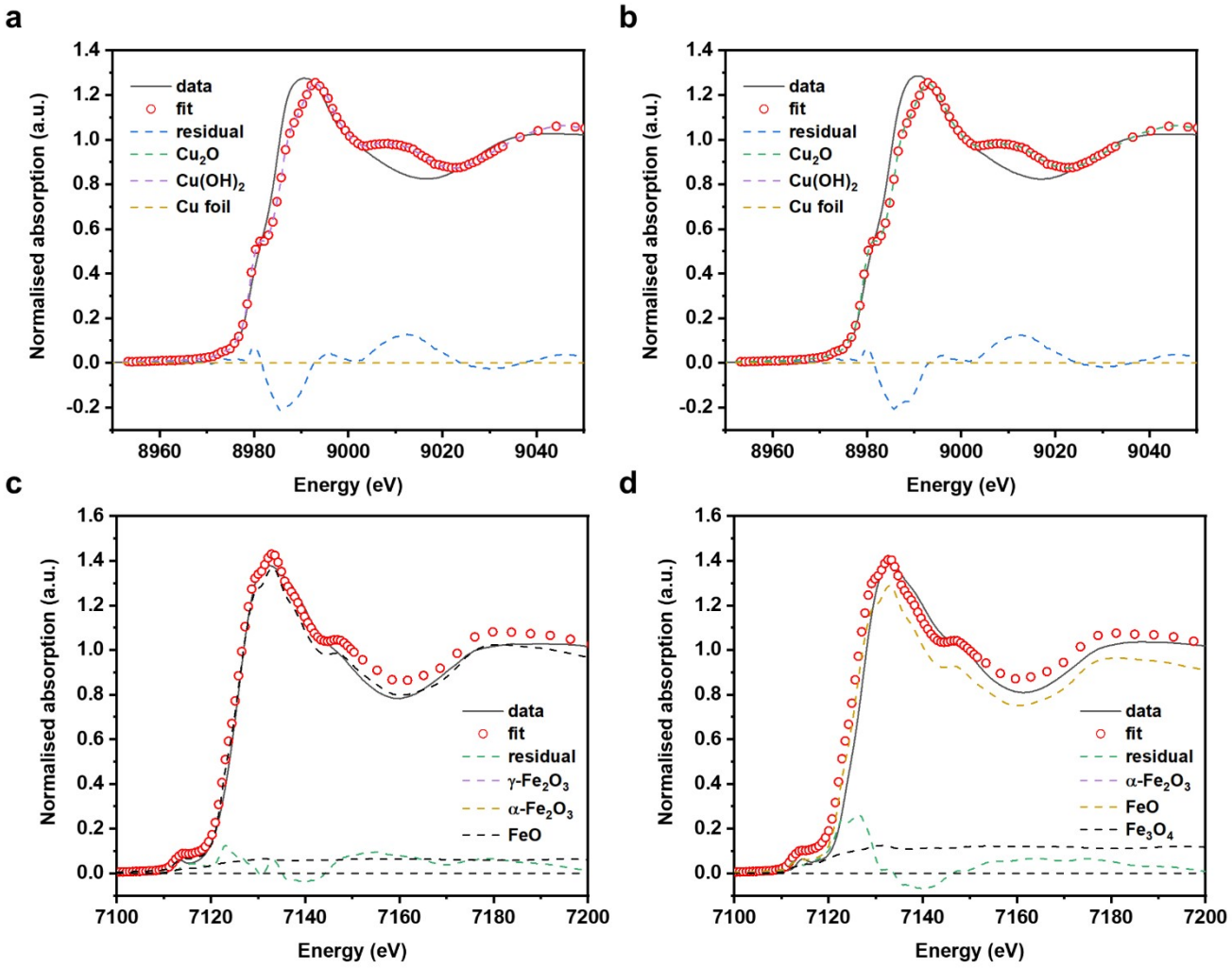

Figure S12. Quantitative fitting analysis of XANES measurements (**a**) **Cu_1-UiO**, (**b**) **Cu,Fe-UiO**, at the Cu K-edge, and (**c**) **Fe_1-UiO**, (**d**) **Cu,Fe-UiO**, at the Fe K-edge.

Table S4(a). Quantitative fitting of the XANES measurements of sample **Cu_1-UiO** and **Cu,Fe-UiO** at the Cu K-edge.

Reference	**Cu_1-UiO**	**Cu,Fe-UiO**
$Cu(OH)_2$	1.00	1.00
Cu_2O	0	0
Cu foil	0	0

Table S4(b). Quantitative fitting of the XANES measurements of sample **Fe_1-UiO** and **Cu,Fe-UiO** at the Fe K-edge.

Reference	**Fe_1-UiO**	**Cu,Fe-UiO**
a-Fe_2O_3	0.99	0.88
FeO	0	0
Fe_3O_4	0	0
Fe foil	0.01	0.12

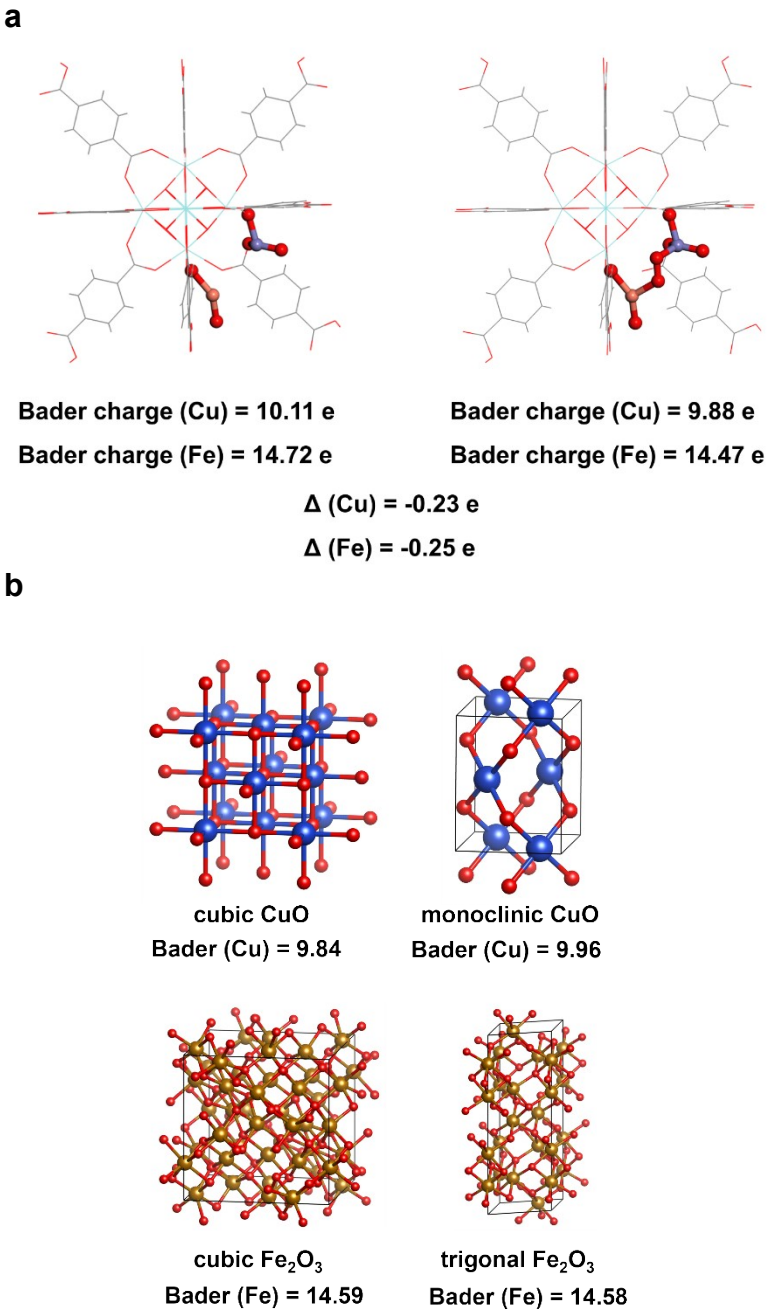

Figure S13. (**a**) Bader charge analysis before and after O_2 attachment over **Cu,Fe-UiO**. (**b**) Bader charge analyses of CuO and Fe_2O_3 presented for comparison.

Table S5(a). Quantitative analysis of the EXAFS results of **Cu,Fe-UiO** at Cu K-edge.

Paths	CN	R (Å)	σ^2 (Å^2)	E_{not} (eV)
Cu-O	3.6(1)	1.95(1)	0.005	-4.1(9)
Cu-Fe	1.0(3)	3.37(1)	0.010	-4.1(9)
Cu-O (2nd shell)	3.2(7)	3.68(1)	0.010	-4.1(9)

Table S5(b). Quantitative analysis of the EXAFS results of **Cu,Fe-UiO** at Fe K-edge.

Paths	CN	R (Å)	σ^2 (Å^2)	E_{not} (eV)
Fe-O	4.6(1)	1.95(1)	0.005	-5.0(4)
Fe-Cu	1.3(3)	3.37(1)	0.010	-5.0(4)
Fe-Fe	0.8(2)	3.04(1)	0.005	-5.0(4)
Fe-O (2nd shell)	5.2(17)	3.68(1)	0.010	-5.0(4)

Table S6(a). Quantitative analysis of the EXAFS results of **Cu_1-UiO** at Cu K-edge.

Paths	CN	R(Å)	σ^2(Å^2)	E_{not} (eV)
Cu-O	3.6(1)	1.95(1)	0.005	-4.2(9)

Table S6(b). Quantitative analysis of the EXAFS results of **Fe_1-UiO** at Fe K-edge.

Paths	CN	R(Å)	σ^2(Å^2)	E_{not} (eV)
Fe-O	3.8(1)	1.99(1)	0.007	-2.1(6)
Fe-Fe	0.4(1)	3.05(1)	0.003	-2.1(6)

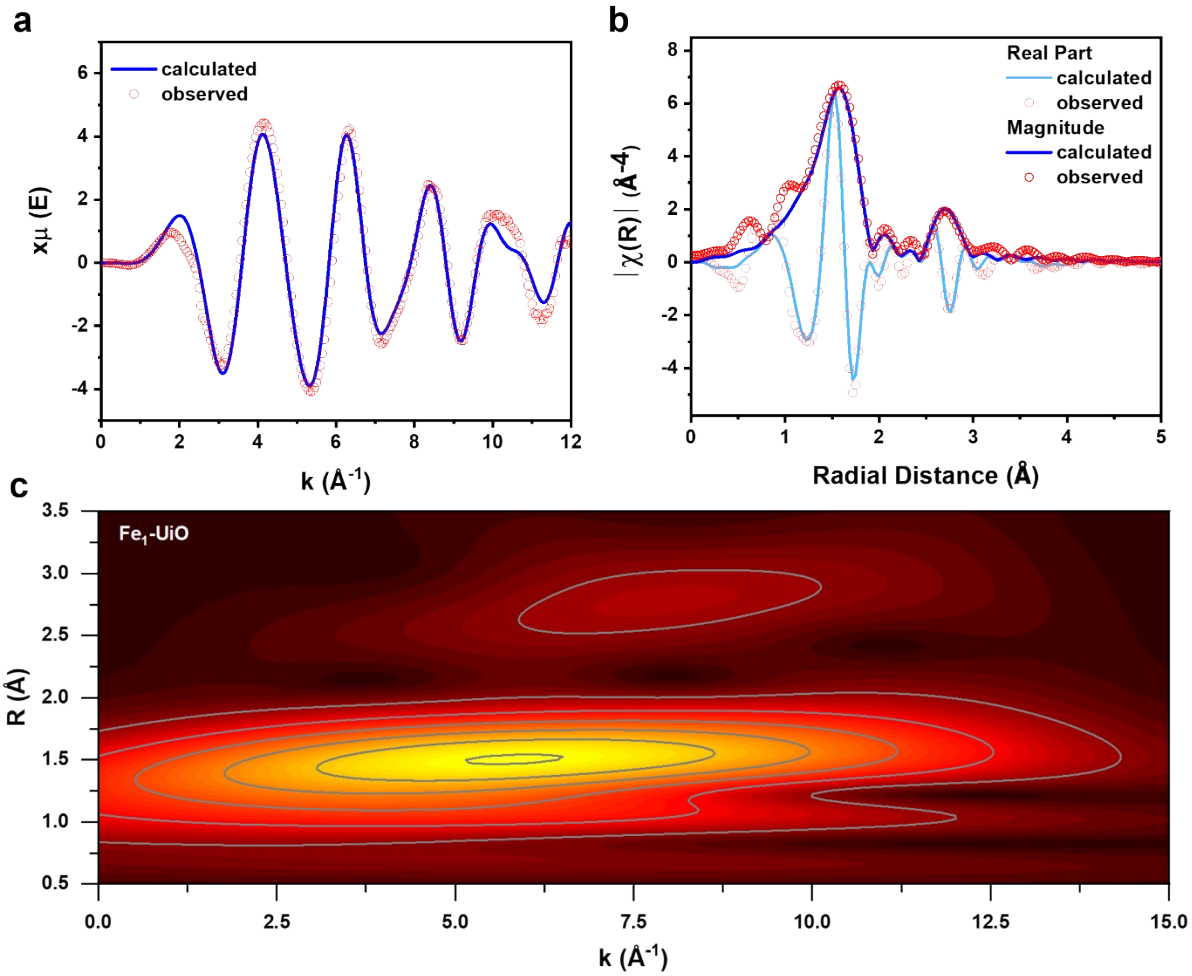

Figure S14. EXAFS data and fitting profiles of **Fe_1-UiO**, (**a**) k-space, (**b**) R-space, and (**c**) wavelet transformation.

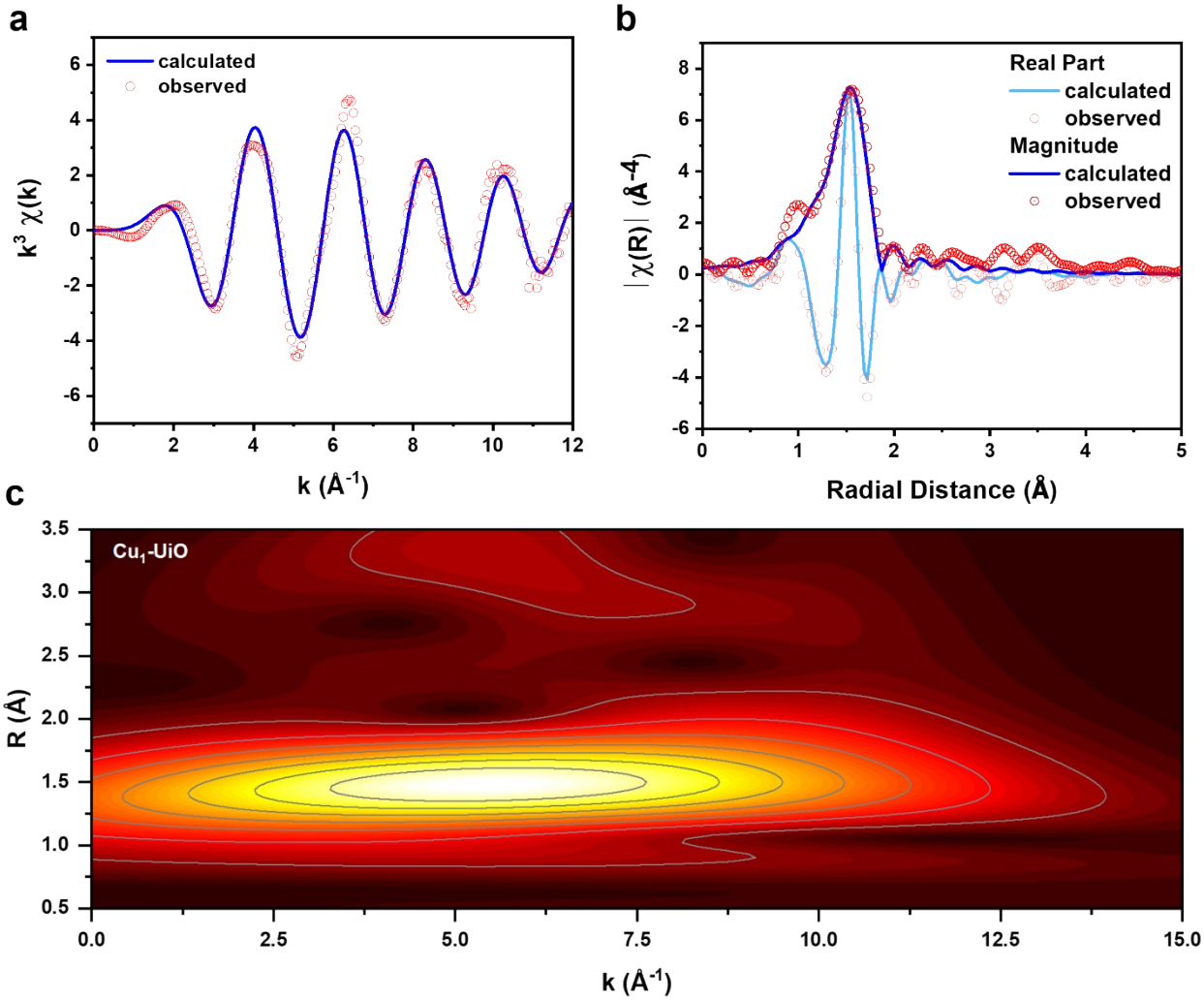

Figure S15. EXAFS data and fitting profiles of **Cu_1-UiO**, (**a**) k-space, (**b**) R-space, and (**c**) wavelet transformation.

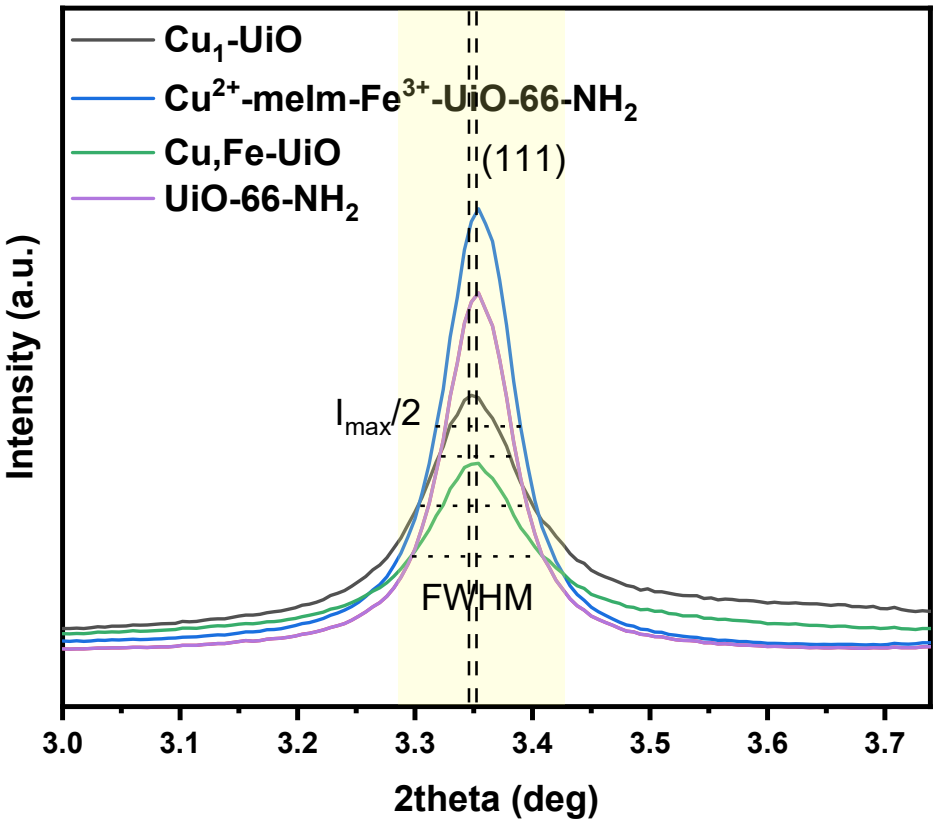

Figure S16. Comparison of the Bragg peak (111) of different samples from synchrotron PXRD measurements. Highly symmetrical peaks before and after metalation can be seen.

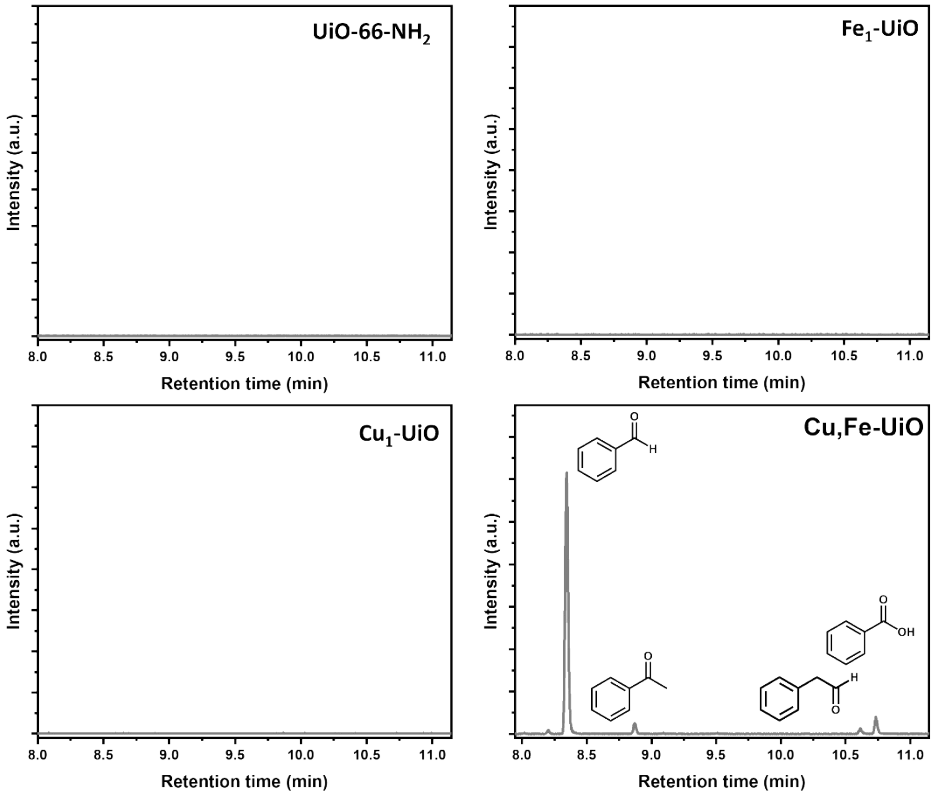

Figure S17. Product distribution from GC-MS of different catalysts. Nil converted aromatic products were observed over UiO-66-NH_2, **Cu_1-UiO** or **Fe_1-UiO**.

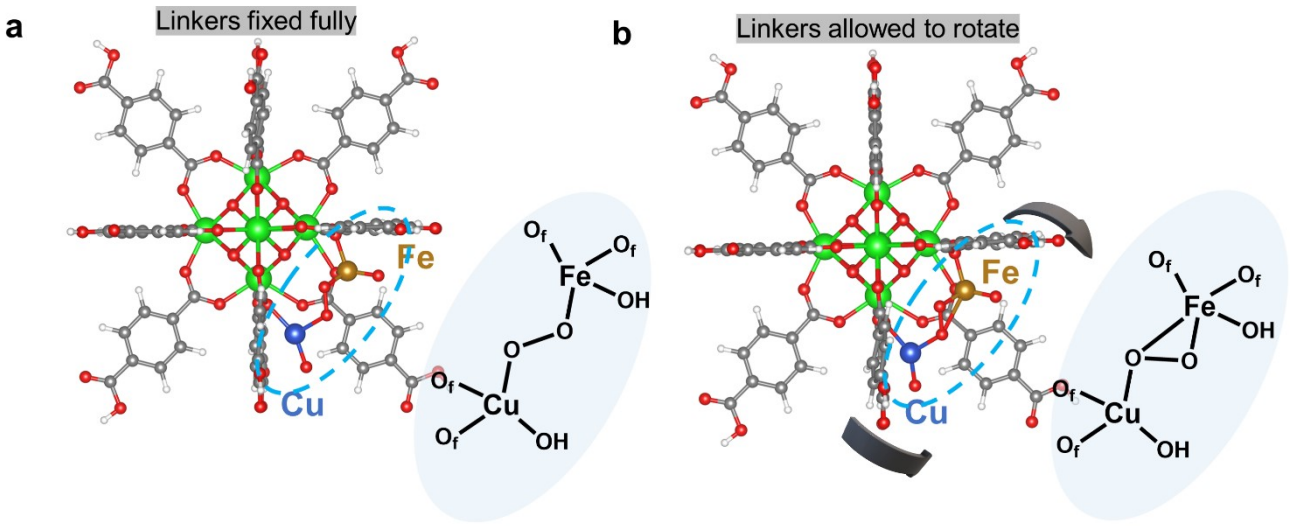

Figure S18. Optimisation of the structure of **Cu,Fe-UiO** by studying the effect of linker rotation.

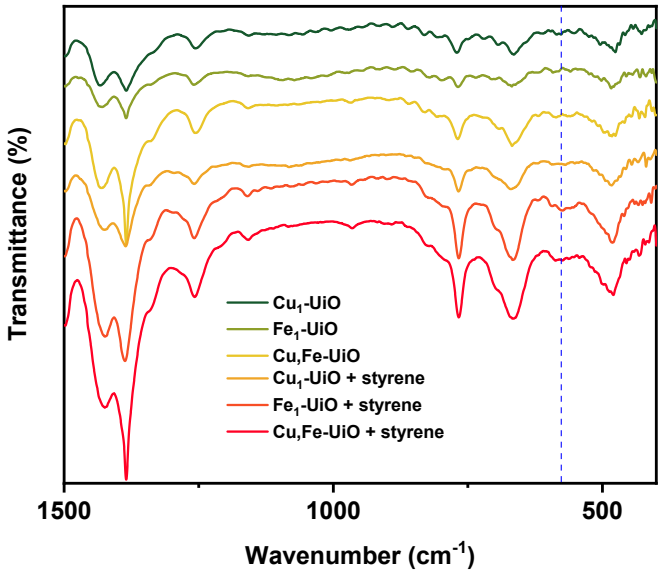

Figure S19. FTIR spectra of samples with and without styrene adsorption.

To investigate the preference in the reaction mechanism (epoxidation pathway versus peroxy pathway), we first employed probe-assisted FTIR to investigate the adsorption property of styrene of **Cu,Fe-UiO**. As seen in **Figure S19**, a band characteristic of Fe–O bond appeared upon the adsorption of styrene. The original FTIR-hidden Fe–O bond became visible, which suggests the interaction between styrene and **Cu,Fe-UiO**.

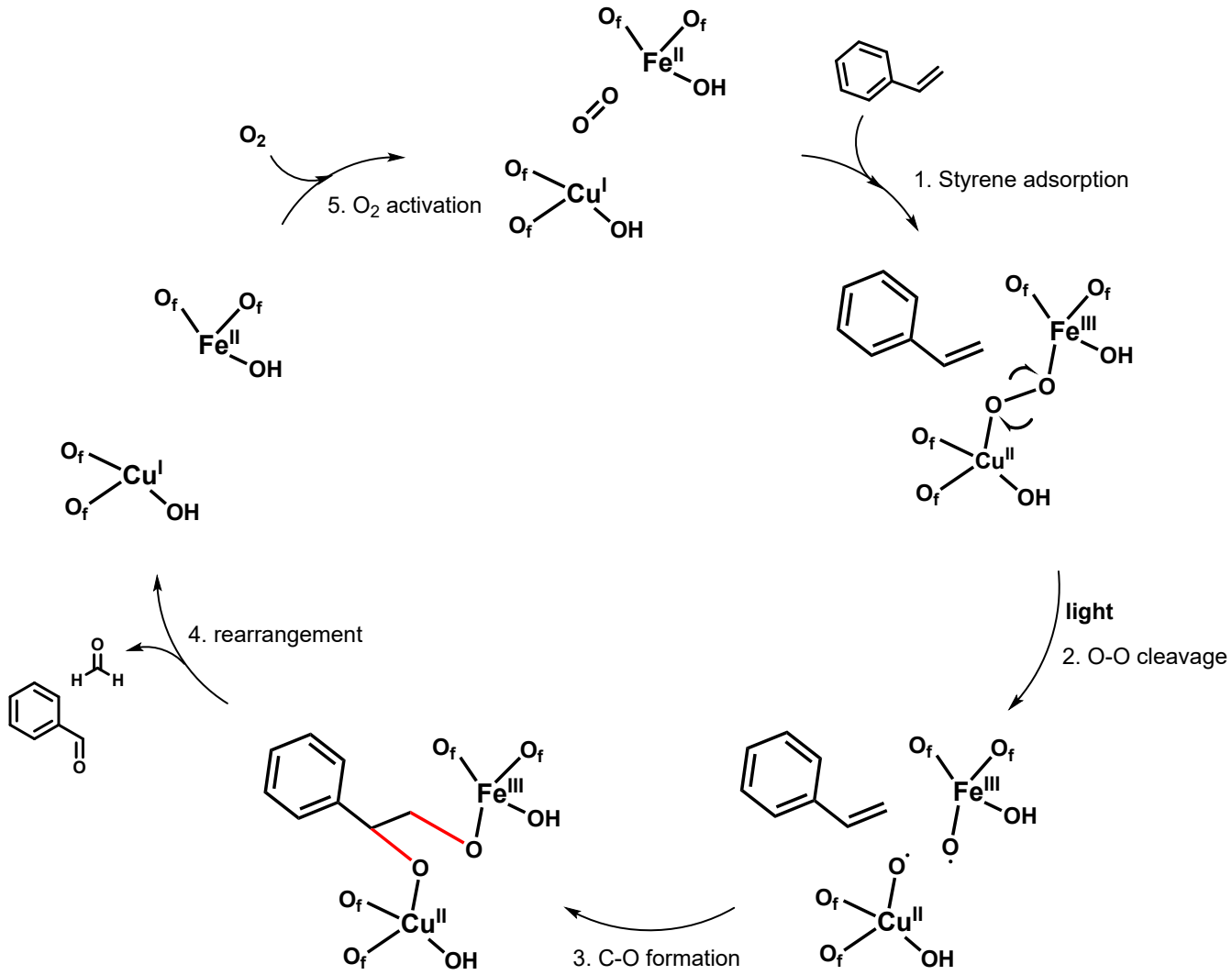

Figure S20. The proposed catalytic cycle of photocatalytic styrene oxidation over **Cu,Fe-UiO**.

Table S7. Atomic parameters derived from the Rietveld refinement of the synchrotron PXRD measurement of **Cu,Fe-UiO**, measured at 25 °C.

Species	Atom	x	y	z	SOF	B_{eq} (Å^2)	Wyckoff letter
MOF-host	Zr1	0.12145	0	0	1	0.6	d
	O2	0.06566	0.06566	0.06566	1	2	f
	C1	0.15679	0	0.15679	1	4	h
	C2	0.20875	0	0.20875	1	4	h
	C3	0.27255	0	0.27255	1	4	j
	O1	0.17288	0	0.09674	1	4	j
	N1	0.28946	0	0.12818	0.25	4	j
Extra-framework site	Cu1	0.0910	0.0910	0.2048	0.069#	5	l
	Fe2	0.0915	0.2048	0.0915	0.074#	5	l
	OCu1	0.1051	0.2952	0.1273	0.069#	5	l
	OFe2	0.1598	0.0909	0.2820	0.074#	5	l
	OB3	0.1341	0.1836	0.1695	0.070	5	l
	OB4	0.1950	0.8910	0.4220	0.070	5	l
Physisorbed water (dummy)	OH1	0.0922	0.0030	0.2714	0.33212	10	l
	OH2	0.0205	-0.0149	0.1217	0.40349	10	l
	OH3	0.0899	-0.0487	0.2752	0.1157	10	l

#: site occupancy factor fixed based on elemental analysis in **Table S1**.

Table S8. The catalytic performance of a series of related and recently reported heterogeneous catalysts.

Catalyst	Oxidative reagent	Conditions	Conversion (%)	Selectivity of benzaldehyde (%)	Reference
MOF-74(Co)	O_2	80 °C	47.3	35	[8]
MOF-74(Cu-90/Co-10)	O_2	80 °C	10.2	75	[8]
MOF-74(Cu-75/Co-25)	O_2	80 °C	17.1	50	[8]
MOF-74(Cu-30/Co-70)	O_2	80 °C	30.4	43	[8]
Pd-Y-bpydc$_{0.8}$/bpdc$_{0.2}$	O_2	80 °C	89	82	[9]
Pd-Y-bpydc$_{0.5}$/bpdc$_{0.5}$	O_2	80 °C	62	86	[9]
Pd-Y-bpydc$_{0.2}$/bpdc$_{0.8}$	O_2	80 °C	45	90	[9]
PW10	$^1O_2$	365 nm at 10 °C	94	80	[10]
Mn-MIL-100	TBHP	70 °C	72.52	82	[11]
Fe-MIL-100	TBHP	70 °C	73.87	76	[11]
Fe-MIL-101	TBHP	70 °C	83.72	68	[11]
Cr-MIL-101	TBHP	70 °C	46.79	91	[11]
Co-MCM-41	H_2O_2	60 °C	36	44	[12]
Ag-MCM-41	H_2O_2	60 °C	29	38	[12]
Ag-Co-MCM-41	H_2O_2	60 °C	45	53	[12]
UiO-66-NH_2@MIL-101(Fe)heterostructures	O_2	> 420 nm	~18	~ 90	[13]
V-Y	TBHP	80 °C	93.35	46	[14]
Mn-Y	TBHP	80 °C	51.06	42	[14]
Fe-Y	TBHP	80 °C	60.94	49	[14]
Co-Y	TBHP	80 °C	82.34	47	[14]
Ni-Y	TBHP	80 °C	90.43	51	[14]
Cu-Y	TBHP	80 °C	88.03	57	[14]
Cu,Fe-UiO	O_2	365 nm at 25 °C	25	92	This work

Y-bpdc: hexanuclear yttrium clusters MOFs
PW10: pyrene-alt-dibenzothiophene-S,S-dioxide (P16PySO)/tungsten trioxide composite
Y: Y-zeolite

References:

1 Q. Xue, Y. Xie, S. Wu, T. S. Wu, Y. L. Soo, S. Day, C. C. Tang, H. W. Man, S. T. Yuen, K. Y. Wong, Y. Wang, B. T. W. Lo and S. C. E. Tsang, *Nanoscale*, 2020, **12**, 23206–23212.

2 C. K. T. Wun, H. K. Mok, T. Chen, T.-S. Wu, K. Taniya, K. Nakagawa, S. Day, C. C. Tang, Z. Huang and H. Su, *Chem Catal.*, 2022, **2**, 2346–2363.

3 T. Chen, Y. Wang, Q. Xue, C. Kit Tommy Wun, P. Kin So, K. Fu Yung, T.-S. Wu, Y.-L. Soo, K. Taniya, S. Day, C. C. Tang, Z. Li, B. Huang, S. Chi Edman Tsang, K. Wong and T. Woon Benedict Lo, *Cell Reports Phys. Sci.*, 2022, **4**, 100850.

4 P. Thompson, D. E. Cox and J. B. Hastings, *J. Appl. Crystallogr.*, 1987, **20**, 79–83.

5 B. Ravel and M. Newville, in *Journal of Synchrotron Radiation*, International Union of Crystallography, 2005, vol. 12, pp. 537–541.

6 H. Funke, A. C. Scheinost and M. Chukalina, *Phys. Rev. B - Condens. Matter Mater. Phys.*, 2005, **71**, 094110.

7 Q. Xue, B. K. Y. Ng, H. W. Man, T. S. Wu, Y. L. Soo, M. M. Li, S. Kawaguchi, K. Y. Wong, S. C. E. Tsang, B. Huang and T. W. B. Lo, *Chem. Sci.*, 2022, **13**, 50–58.

8 Y. Fu, L. Xu, H. Shen, H. Yang, F. Zhang, W. Zhu and M. Fan, *Chem. Eng. J.*, 2016, **299**, 135–141.

9 Y. Zhang, N. Wei, Z. Xing and Z.-B. Han, *Appl. Catal. A Gen.*, 2020, **602**, 117668.

10 C. Cheng, B. Zhu, B. Cheng, W. Macyk, L. Wang and J. Yu, *ACS Catal.*, 2022, **13**, 459–468.

11 Y. Ha, M. Mu, Q. Liu, N. Ji, C. Song and D. Ma, *Catal. Commun.*, 2018, **103**, 51–55.

12 T. Jiang, G. Gao, C. Yang, Y. Mao, M. Fang and Q. Zhao, *J. Nanosci. Nanotechnol.*, 2020, **20**, 1670–1677.

13 L. Liu, L. Zhang, F. Wang, K. Qi, H. Zhang, X. Cui and W. Zheng, *Nanoscale*, 2019, **11**, 7554–7559.

14 N. C. Desai, J. A. Chudasama, T. J. Karkar, B. Y. Patel, K. A. Jadeja, D. R. Godhani and J. P. Mehta, *J. Mol. Catal. A Chem.*, 2016, **424**, 203–219.